Journal of
Nanoscience and Nanotechnology
Vol. 9, 3853–3857, 2009

Nano Si Superlattices for the Next Generation Solar Cells

B. Pivac[1,*], P. Dubček[1], I. Capan[1], I. Zulim[2], T. Betti[2], H. Zorc[1], and S. Bernstorff[3]

[1]*Ruđer Bošković Institute, P.O. Box 180, 10000 Zagreb, Croatia*
[2]*FESB, University of Split, R. Boškovića b.b., 21000 Split, Croatia*
[3]*Sincrotrone Trieste, Strada Statale 14, km 163.5, 34012 Basovizza (Trieste), Italy*

We present a study on amorphous SiO/SiO_2 superlattice formation on Si substrate held at room temperature and annealed in the temperature range 600–1100 °C. Grazing-incidence small-angle X-ray scattering (GISAXS) and X-ray reflectivity were used to study such samples. Amorphous SiO/SiO_2 superlattices were prepared by high vacuum physical vapor deposition of 4 nm thin films of SiO and SiO_2 (10 layers each) from corresponding targets on silicon substrate. Rotation of the Si substrate during evaporation ensured homogeneity of the films over the whole substrate. We observed that the inhomogeneities introduced into the SiO and SiO_2 layers during the deposition (evaporation) give rise to small angle scattering at lower annealing temperatures. After an initial SiO layer thickness reduction for 600 °C annealing, these thicknesses remain virtually unchanged up to 1000 °C, where they start to decrease again which leads to particle formation. Nevertheless, this compacting at low temperatures may lead to the seed formation in SiO layers that will facilitate later Si nanoparticles growth.

Keywords: Si Nanostructures, SiO/SiO_2 Amorphous Superlattice, Small Angle X-ray Scattering, Synchrotron Radiation, Solar Cells.

RESEARCH ARTICLE

1. INTRODUCTION

The most recent developments in photovoltaic technologies aiming to reduce the cost of production explore the new possibilities offered by inovative concepts in the nanotechnology. The concept is to engineer the band structure of silicon by formation of silicon nanocrystals embedded in either a SiO_2 or a Si_3N_4 matrix. Nanocrystals less than 7 nm in diameter behave as quantum dots exhibiting quantum confinement. If such formed Si nanocrystals are placed close enough to each other, the overlap of the wavefunctions of quantum confined carriers in adjacent dots can contribute to the formation of a true superlattice with the confined states smeared out to form a mini-band.[1]

Recently, many alternative techniques for the synthesis of Si nanocrystallites in oxide matrix were explored such as high dose Si-ion implantation in SiO_2,[2] cosputtering of Si and SiO_2,[3] or cosputtering of SiO and SiO_2,[4] laser ablation of Si, solely or together with SiO_2,[5] gas-phase evaporation of SiO,[6] and plasma-assisted chemical vapor deposition of silicon suboxide.[7] Another powerful technique for producing Si nanocrystallites in a SiO_2 matrix is thermal evaporation of SiO or SiO and SiO_2.[8–10]

A new method based on the preparation of SiO/SiO_2 superlattices which enables the independent control of size, size distribution, position and density of the nanocystals was suggested.[11,12] However, the diffusion and phase separation process in such confined geometries and in the presence of SiO_2 nearby the interface is not yet completely understood. In addition there is no theoretical work available to our best knowledge, which describes both the phase separation and the crystallization process in the limit of ultrathin layers. For a better understanding of that problem, it is necessary to learn more about the structural changes occurring during the annealing of such superlattices, which we shall present in this work.

2. EXPERIMENTAL DETAILS

Amorphous SiO/SiO_2 superlattices were prepared by high vacuum evaporation of alternating films of SiO_2 and SiO, each 4 nm thick (forming a stack of 10 bilayers) on clean Si(100) substrate held at room temperature. Rotation of the Si substrate during evaporation ensured uniformity of the films over the whole substrate surface. After deposition, the samples were annealed from 600 °C to 1100 °C for 1 h in vacuum better than 10–2 Pa to induce Si nanocrystals formation.

X-ray reflectivity (XRR) measurements were performed at the ELETTRA synchrotron radiation source, Trieste (Italy), at the SAXS beamline[13] using a X-ray beam energy of 8 keV ($\lambda = 0.154$ nm). The size of the incident beam

*Author to whom correspondence should be addressed.

1533-4880/2009/9/3853/005 doi:10.1166/jnn.2009.NS79

was 5 mm × 0.1 mm (horizontal × vertical). The stage (and the sample surface) was aligned horizontally and parallel to the incoming beam within ±0.1°. The scattered intensity was measured using a Gabriel type, gas filled 1D detector at a fixed position (this corresponds to the so-called detector scans taken with a point detector). For each sample, the scattered intensity has been measured in the whole grazing angles range from below the critical angle, which is 0.23° for silicon, up to 2° approximately. The X-ray reflectivity has been extracted from these measurements as the specular peak integral intensity, with the diffuse intensity subtracted.[14] There are several other ways to handle reflectivity results, e.g., Ref. [15] which are however less suitable for our type of samples.

Grazing incidence small angle X-ray scattering (GISAXS) experiments were also carried out at the synchrotron facilities of Elettra, using synchrotron radiation with wavelength $\lambda = 0.154$ nm (photon energy of 8 keV). The grazing angle of incidence was selected in the range $0.3° < \alpha_i < 1.4°$ for which the effective area of the beam foot print is smaller than the sample surface area (20 mm × 20 mm); the incident angle α_i was larger than the critical angle for total external reflection of the silicon substrate $\alpha_{crit}(Si) = 0.23°$. A two dimensional CCD detector with 1024 × 1024 pixels, positioned perpendicular to the incident beam at a detector to sample distance $L = 2000$ mm, was used to record the SAXS intensity. A thin Al-strip was placed in front of the 2D detector to avoid saturation in the specular plane direction where the usually much stronger surface scattering is present. The spectra were corrected for the background intensity and detector response.

3. RESULTS AND DISCUSSION

X-ray reflectivity from a rough surface in the limit of small surface roughness (i.e., $q_z^2\sigma^2 \ll 1$, where q_z is the scattering wavevector in the direction perpendicular to the surface and σ is the surface roughness), is given in the framework of the distorted wave Born approximation (DWBA) as

$$|r|^2 = |r_F|^2 \exp[-q_z q_z' \sigma^2] \quad (1)$$

where q_z' and q_z are the scattering wavevectors in and outside the solid surface, respectively, and r_F is the Fresnel reflectivity. In the approximation of small angles, the latter is given by

$$r_F = \frac{q_z - q_z'}{q_z + q_z'} \quad (2)$$

However, when X-rays impinge on the surface of a thin film placed on a substrate with index of refraction different from that of the substrate, the part of the beam transmitted through the upper film surface gets partly reflected on the lower one. Then it reaches the upper surface from below and is partly transmitted, contributing additionally to the overall reflectivity. The part that is reflected from the upper surface back into the film repeats the same sequence of reflection (from the lower surface) and transmission (through the upper surface). This transmission-reflection sequence is repeated endlessly, and then the reflectivity can be summed into

$$r = \frac{1}{r_1 r_2 + 1} \quad (3)$$

Here, r_1 and r_2 are the reflectivities on the top and the bottom film surface, respectively. This can be easily extended to an N-layered film where the index of refraction of each layer differs from that of the adjacent ones. The coefficient of reflection of each layer is calculated separately as

$$R = \frac{R_{j+1} + r_j}{R_{j+1} r_j + 1} \quad (4)$$

where R_j is the reflectivity in the jth sublayer (from the jth interface) with the multiple reflections included, while r_j is the Fresnel type reflectivity from the jth interface, given by Eq. (2). The substrate is very thick compared to the film, therefore the intensity reflected from its bottom is neglected ($R_N = 0$). Thus, if we start from the substrate surface we can calculate the reflectivity in each layer progressively towards the film surface using Eq. (4). Finally, the film reflectivity, with all the layer contributions included, is obtained as RMS value of the reflectivity from the top layer R_0:

$$R = \frac{I_R}{I_0} = |R_0|^2 \quad (5)$$

where I_R and I_0 are the reflected and the incoming intensity.

The measured X-ray reflectivities for the as prepared sample and those annealed at different temperatures are shown in Figure 1 as open circles, together with the calculated reflectivities shown as solid curves and obtained by fitting using the above described calculation procedure. The annealing temperatures are also shown in the figure. Since our samples are stacks of 10 bilayers, one would expect Bragg type reflections to occur at odd indexes. Namely, when both layers in a bilayer are of the same thickness the Bragg peaks at even indexes should be absent. The first one is visible at about $q = 0.8$ nm^{-1}, but the third one at $q = 2.4$ nm^{-1} is apparently missing. The relatively weak first Bragg peak could be attributed to a small difference in electron density of the evaporated SiO and SiO_2, but the absence of the third Bragg peak suggests that the roughness of the interfaces between the layers is also significant.

If we follow the strength of the first Bragg peak in Figure 1, we can see that it gets stronger after annealing at 600 °C, and weakens again after annealing above 1000 °C. The fringes that are present in all reflectivity curves can be a good measure of the overall film thickness. Their dominance in the reflectivity curves suggests that the electron densities of SiO and SiO_2 are similar and significantly

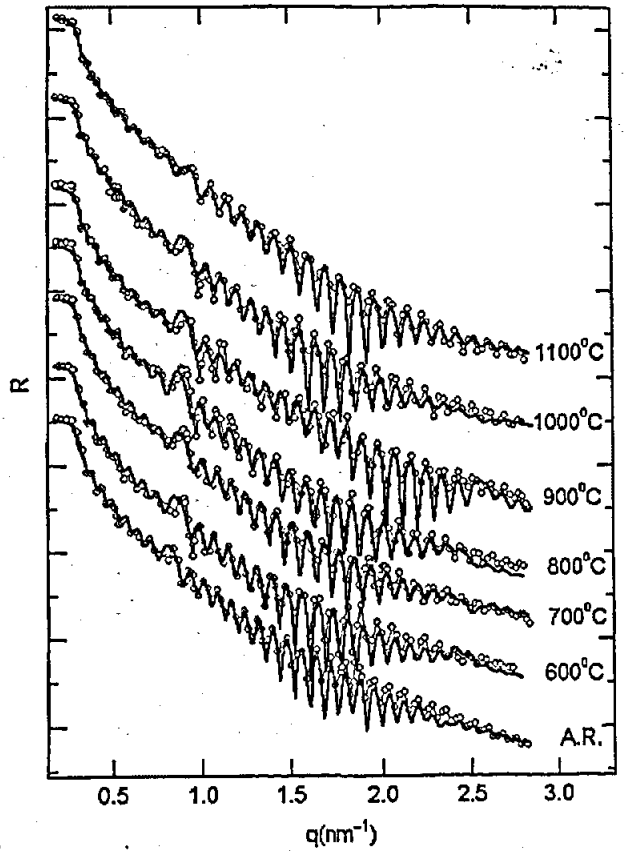

Fig. 1. X-ray reflectivity (open circles) for 10 SiO/SiO_2 bilayers together with the best fit (full lines) as a function of the grazing wave vector. The annealing temperatures are indicated at the corresponding curves, and the curves are offset vertically for the sake of clarity.

lower than the density of the substrate (monocrystalline silicon).

Our samples are stacks of the same 10 bilayers of amorphous SiO/SiO_2 that have been annealed at different temperatures. We can assume that the number of electrons in each layer is constant, and only the change of layer thickness can affect the index of refraction. Namely, at lower temperatures of annealing the amorphous structure of the films is relaxed, and at high temperatures a phase separation takes place, as described by

$$SiO_x \rightarrow \frac{x}{2}SiO_2 + \left(1-\frac{x}{2}\right)Si \qquad (6)$$

In our case $x = 1$. On the other hand, the density of both SiO and SiO_2 is expected to be smaller than the standard value for the bulk materials. Therefore the layer density becomes a function of its thickness and not a free fitting parameter. For the layer roughness we adopted the simplest model: it was increasing linearly from the substrate towards the surface of the film, starting from an initial value higher than that of the substrate, which, in turn, is a very low value typical for monocrystalline silicon.

In Figure 2 the thickness of the SiO and SiO_2 layers is plotted as a function of the annealing temperature. These values were obtained by fitting.

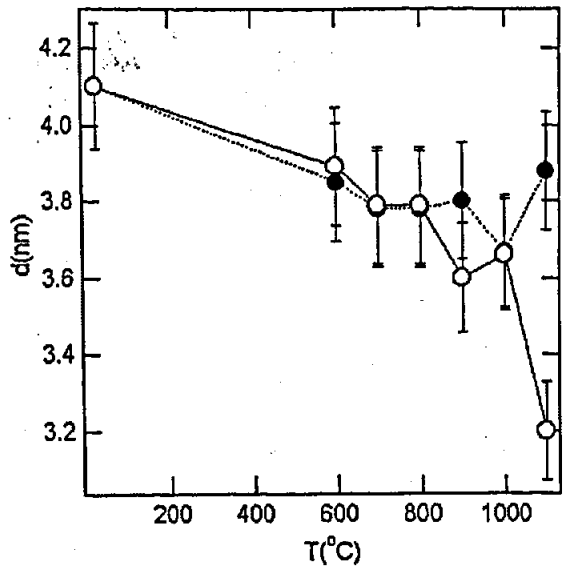

Fig. 2. Thickness of SiO (open circles) and SiO_2 (full circles) as a function of annealing temperature.

The relatively big error bars are partly misleading: from the big number of fringes obtained for this angular range, the overall thickness of the film can be determined very precisely, and the Bragg peak position is giving the bilayer thickness precisely, too. It is the thickness of each layer in the bilayer that is harder to obtain.

Nevertheless, we can follow the initial relaxation of the structure, evident as the reduction of the layer thicknesses at 600 °C, and partly also at 700 °C. After that those thicknesses are more or less unchanged up to the highest annealing temperature, where the thickness of the SiO layers suddenly drops and that of the SiO_2 layers increases again. The gross change of the whole film thickness is towards lower values: the increment in the SiO_2 layer thickness is less than the decrement in the SiO layer. This is expected from the values of the bulk densities: following Eq. (6) (the number of silicon and oxygen atoms stays the same) one finds that the separated Si atoms and SiO_2 molecules occupy less space than the originally present SiO molecules. One would expect this to hold also for the surface evaporated material as well.

In Figure 3. the roughness of the layers is plotted as a function of the annealing temperature. We supposed that the roughness of the layers is dominantly a function of the preparation method and that it is relatively high initially. Successive layer evaporation increases the surface roughness, but at a lesser rate. Therefore, the roughness was supposed to increase for an additional 0.05 nm for each bilayer progressively towards the film surface, while the value for the initial bilayer is the one plotted in Figure 3. Varying the rate of increment of the roughness together with the initial value did not result in an improvement of the fit, and the 0.05 nm per bilayer was chosen to be common.

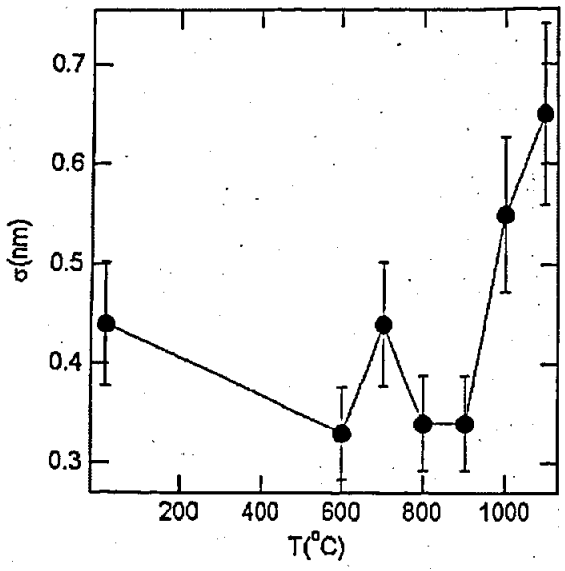

Fig. 3. Roughness of the lowest layer in the film as a function of the temperature as obtained from fitting.

The roughness of the layers is reduced slightly during the 600 °C annealing due to structural relaxation (the Bragg peak gets enhanced compared to the one from as the received sample) although the consequence of the relaxation is not as clearly resolved as in the case of the sample thickness in Figure 2. It is increased again, this time significantly after annealing at 1000 °C or higher temperatures.

The phase separation given by Eq. (6) is expected to happen at 1100 °C in every other SiO layer.[12] Since SiO_2 is a barrier to silicon diffusion, this phase separation combined with confinement due to adjacent SiO_2 layers it should result in Si nanoparticle formation within the SiO layer.

What we have observed by X-ray reflectivity is a destruction of the SiO layer: its thickness is reduced to the benefit of the SiO_2 layer thickness and its roughness is increased. The initial SiO layer thickness was chosen in order that the diffusing silicon would form nanoparticles of similar size positioned at the center of the ex SiO layer.

We performed GISAXS experiments in order to verify that silicon particles have been formed. A 2D CCD detector was used and a typical pattern for the sample annealed at 1100 °C is shown in Figure 4. The grazing angle was $\alpha_c + 0.1°$ to allow for the scattering contribution from within the film, since the penetration depth corresponds to the sample thickness at this grazing angle.

The scattering is still dominated by the surface roughness contribution, which includes the scattering from all the interfaces between the different layers throughout the sample. At $q_z = 0.3$ nm^{-1}, a broadened Yoneda type of scattering can be observed. This is the position where the evanescent signal from the sample leaves the sample surface at an angle equal to the critical angle. In the vicinity of the specular peak ($q_y = 0$), at about $q_z = 0.9$ nm^{-1}, a broadening of the Bragg peak, that is due to the bilayered

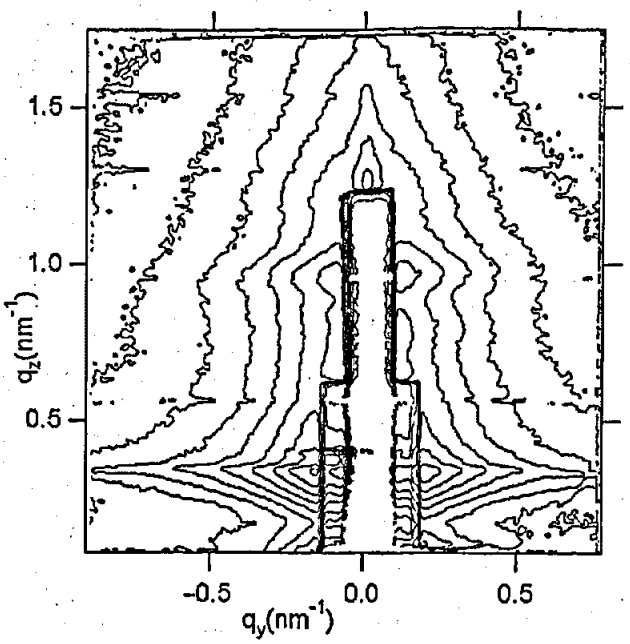

Fig. 4. GISAXS scattering from the sample annealed at 1100 °C, taken at the grazing angle $\alpha = \alpha_c + 0.1°$, shown in contour plot.

sample structure and has been already discussed in the reflectivity section, can be observed. Since the thickness of the SiO_2 layer is small, a rather strong interaction of the Si nanoparticles growing in adjacent layers is expected. In the case when the size of these particles equals the thickness of the SiO layer, its lateral shift is favored for the particle in the adjacent layer.[10] As a result, particles growing in

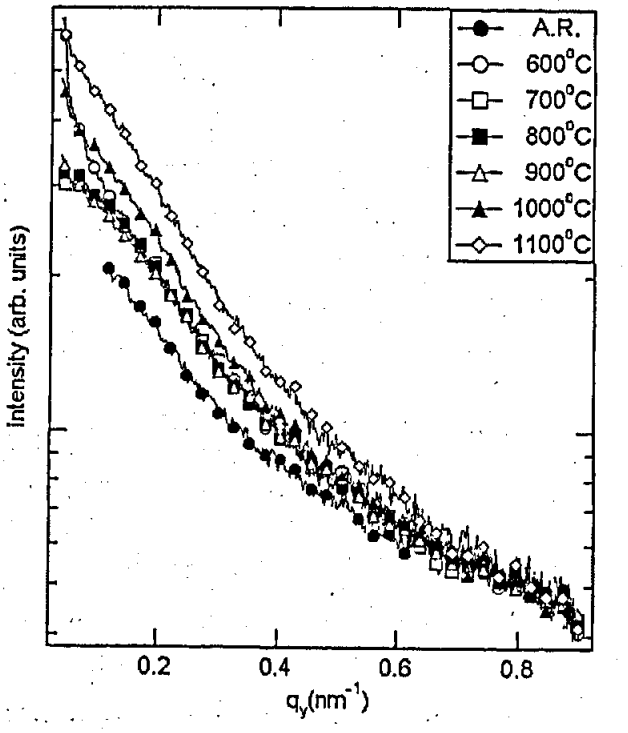

Fig. 5. 1-D scattering intensities taken at $q_z = 1.3$ nm^{-1} (see Fig. 4.) vresus the scattering wave vector in the direction parallel to the sample surface. The annealing temperatures are indicated in the insert.

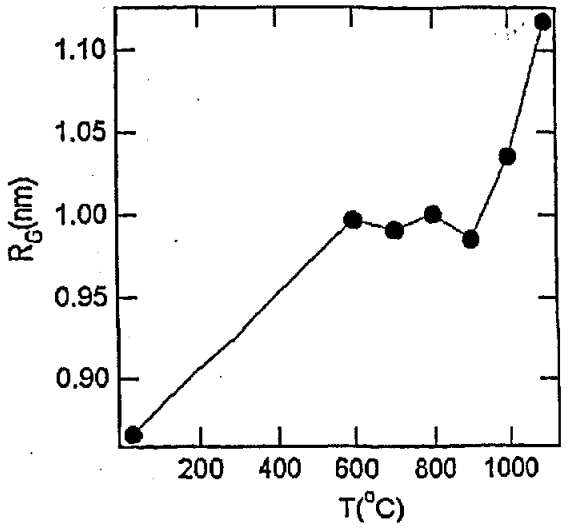

Fig. 6. Radius of gyration obtained from the Guinier fit of the data in Figure 5. versus annealing temperature.

every second or third layer, would be correlated vertically, resulting in a correlation maximum appearing in GISAXS at angles below the Bragg peak position.

The absence of the correlation peak reveals a poor vertical correlation. However, when the intensities along $q_z = 1.3$ nm^{-1} are plotted, we can clearly see a difference in the diffuse scattering, as shown in Figure 5. The scattering intensities are apparently very similar for all annealing temperatures, only for the as received and the 1100 °C annealed sample they differ. Without going into details of the origin of the scattering, one can conclude that the lower annealing temperatures cause structural relaxation (hence the lower intensity from the as received sample), and only at 1100 °C the particles are actually formed, although distributed quite irregularly through the ex SiO layer.

The shape of the curves also suggests that a range of sizes is present in the sample. If we apply a simple Guinier fit to obtain qualitative information of the sizes dependence on the temperature, we notice the trend illustrated in Figure 6. At the intermediate temperatures of annealing particle did not grow, and the growth started only at elevated temperatures.

4. CONCLUSIONS

Inhomogeneities are introduced into the SiO and SiO_2 layers during the deposition (evaporation) and these give rise to small angle scattering at lower annealing temperatures. After an initial layer thickness change for 600 °C annealing, these thicknesses remain virtually unchanged up to 1000 °C, where they start to decrease. Furthermore, in this intermediate temperature range no significant growth of nanoparticles is observed. However, this compacting upon annealing at intermediate temperatures may lead to the seed formation in SiO layers that will facilitate later growth. Further studies are needed to explore this subject in greater details.

References and Notes

1. G. Conibeer, M. Green, R. Corkish, Y. Cho, E.-C. Cho, C.-W. Jiang, T. Fangsuwannarak, E. Pink, Y. Huang, T. Puzzer, T. Trupke, B. Richards, A. Shalav, and K. Lin, *Thin Solid Films* 511–512, 654 (2006).
2. V. Lehmann and U. Goesele, *Appl. Phys. Lett.* 58, 856 (1991).
3. S. Hayashi, Y. Kanazawa, T. Kageyama, S. Takeoka, M. Fuji, and K. Yamamoto, *Solid State Commun.* 102, 533 (1997).
4. S. Bernstorff, P. Dubček, I. Kovačević, N. Radić, and B. Pivac, *Thin Solid Films* 515, 5637 (2007).
5. K. Murakami, T. Suzuki, T. Makimura, and M. Tamura, *Appl. Phys. A* 69, S13 (1999).
6. H. Hofmeister and P. Koedderitzsch, *Nanostruct. Mater.* 12, 203 (1999).
7. F. Iacona, G. Franzo, and C. Spinella, *J. Appl. Phys.* 87, 1295 (2000).
8. U. Kahler and H. Hofmeister, *Appl. Phys. A* 74, 13 (2002).
9. B. Pivac, I. Kovačević, P. Dubček, N. Radić, and S. Bernstorff, *Thin Solid Films* 515, 756 (2006).
10. I. Kovačević, P. Dubček, S. Duguay, H. Zorc, N. Radić, B. Pivac, A. Slaoui, and S. Bernstorff, *Physica E* 38, 50 (2007).
11. L. Tsybeskov, K. D. Hirschman, S. P. Duttagupta, M. Zacharias, P. M. Fauchet, J. P. McCafrey, and D. J. Lockwood, *Appl. Phys. Lett.* 72, 43 (1998).
12. M. Zacharias, J. Heitmann, R. Scholz, U. Kahler, M. Schmidt, and J. Blaesing, *Appl. Phys. Lett.* 80, 661 (2002).
13. H. Amenitsch, S. Bernstorff, and P. Laggner, *Rev. Sci. Instrum.* 66, 1624 (1995).
14. S. K. Sinha, *Physica B* 173, 25 (1991).
15. S. Dourdain, J.-F. Bardeau, M. Colas, B. Smarsly, A. Mehdi, B. Ocko, and A. Gibaud, *Appl. Phys. Lett.* 86, 113108 (2005).

Received: 10 July 2007. Accepted: 12 October 2007.

RESEARCH ARTICLE